nature physics

Article

https://doi.org/10.1038/s41567-026-03335-y

Phonon focusing at room temperature

Received: 14 July 2025

Accepted: 19 May 2026

Published online: 23 July 2026

Check for updates

Man Li[1,5], Huan Wu[1,5], Zihao Qin[1,5], Chuanjin Su[1], Huu Duy Nguyen[1] & Yongjie Hu[1,2,3,4]

Wavelike heat transport in solids, known as phonon focusing, has so far been observed only at cryogenic temperatures, limiting both its investigation and potential applications. Here we demonstrate phonon focusing at room temperature in boron arsenide, a material with high thermal conductivity. The measured ray-like temperature patterns and heat propagation dynamics match with first-principles Boltzmann transport simulations. We show that the observed heat dynamics originate from the spatial redistribution of non-equilibrium phonon waves with long propagation lengths. Moreover, our first-principles theory identifies distinct transport symmetries governed by crystallographic orientation, which we experimentally validate across multiple samples. These findings offer opportunities for directional and nanoscale control of phonon waves, non-equilibrium phonon distributions, and phonon–carrier interactions for next-generation thermal and quantum technologies at room temperature.

Phonon focusing is one of the most exotic phenomena in heat-transport physics[1–3]. In non-metallic solids, phonons—quantum mechanical modes of lattice waves—are the primary carriers of heat. Typically, phonons disperse heat in all directions, continuously spreading thermal energy throughout a material, as described by the well-established principles of heat conduction found in textbooks[4]. Nevertheless, phonons exhibit an inherent wave-particle duality, and fundamental wave propagation could emerge under minimum scattering[5], providing the possibility to direct sound or heat[6,7], analogous to the way light is focused through a lens and guided along specific paths, as seen in applications ranging from eyeglasses to telescopes. However, observing phonon focusing in heat transport is particularly challenging, because heat conduction involves broadband phonons that extend beyond terahertz frequencies and possess short wavelengths. This makes temperature effects far more elusive than acoustics or ultrasound, where only low-energy acoustic phonons near the Brillouin zone centre are excited and contribute[8].

The exploration of phonon focusing in heat transport has been scarce so far, and restricted to cryogenic temperatures. The earliest and only temperature measurements date back to the 1970s[1–3], where delicate experiments using a superconducting bolometer were conducted to detect heat pulses at extremely low temperatures ranging from 1.8 to 3.6 K. At these low temperatures, phonons can travel long distances without scattering, allowing their wave-like nature to become more pronounced. At higher temperatures, the increased population of phonons and their more frequent scatterings (with other phonons, lattice imperfections, defects and so on) result in frequent energy and momentum exchanges, disrupting phonon waves and causing thermal energy to become more diffusive, resembling classical heat conduction. The rarity of the observation of phonon focusing and its limitation to low temperatures have impeded its scientific exploration and potential applications over the past several decades. Despite these challenges, understanding fundamental wave behaviours and the potential for precise control of heat flow and thermal properties is crucial for enabling new approaches in electronics thermal management, materials design and advanced quantum devices[9–14]. In this Article, we report the experimental observation of phonon focusing in heat transport at room temperature, revealed through phonon-focusing-induced temperature patterns measured by nanoscale temperature imaging and explained by first-principles theoretical analysis. This discovery not only confirms the existence of room-temperature phonon heat waves, but also opens new possibilities for directionally controlling heat transport at the nanoscale, tailoring the phonon density of states,

[1]Department of Mechanical and Aerospace Engineering, University of California, Los Angeles, CA, USA. [2]California NanoSystems Institute, University of California, Los Angeles, CA, USA. [3]Department of Materials Science and Engineering, University of California, Los Angeles, CA, USA. [4]Center for Quantum Science and Engineering, University of California, Los Angeles, CA, USA. [5]These authors contributed equally: Man Li, Huan Wu, Zihao Qin.
e-mail: yhu@seas.ucla.edu

https://doi.org/10.1038/s41567-026-03335-y

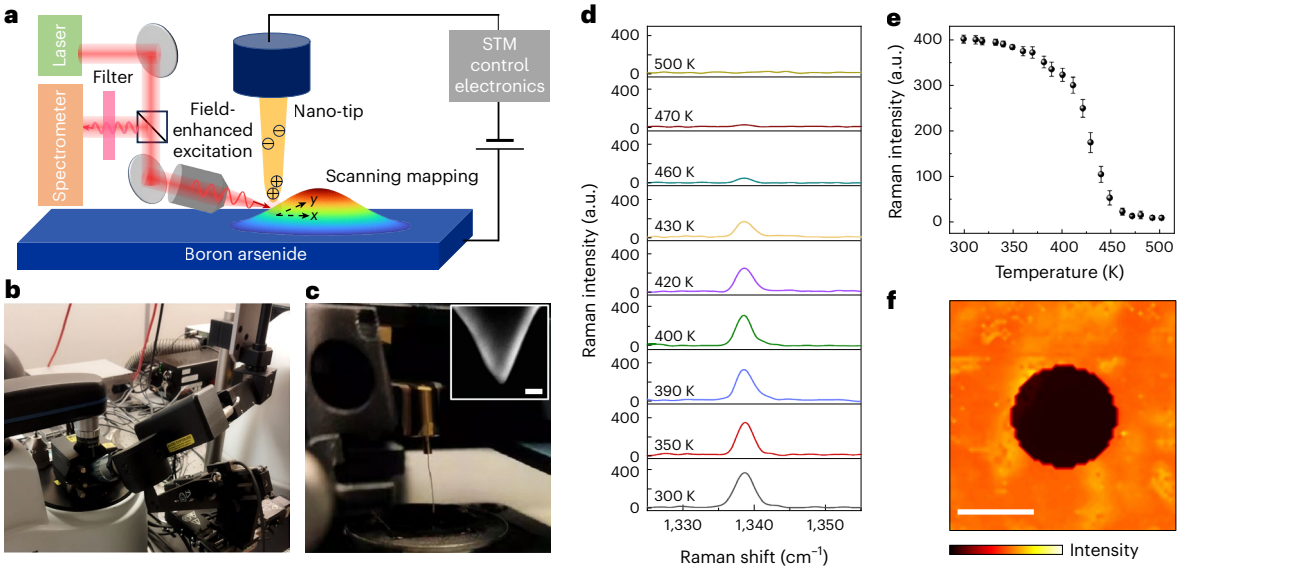

Fig. 1 | Experimental set-up for the nanoscale temperature-mapping technique based on tip-enhanced Raman spectroscopy. a, Schematic illustration of the experiment. Localized heating is induced by a nanoscale tip, and the resulting temperature profiles are characterized by measuring the surface morphology resulting from thermal desorption of surrounding single-layer molecules using tip-enhanced Raman spectroscopy. **b**,**c**, Images of the STM-controlled experimental system, showing the excitation laser (**b**) and the scanning probe with a nanoscale tip (**c**). Inset: scanning electron microscopy image of the gold tip. Scale bar, 100 nm. **d**, Raman spectra of self-assembled single-layer molecules measured at different temperatures. **e**, Temperature-dependent Raman intensity of the characteristic Raman peak measured from ten independent samples. Error bars represent standard deviations, and centre values indicate the mean. **f**, Two-dimensional imaging of a gold film, revealing a circular temperature profile characteristic of diffusive heat conduction. The colour scale denotes Raman intensity in arbitrary units, increasing from low (dark red) to high (yellow). Scale bar, 100 nm.

engineering non-equilibrium phonon distributions, and manipulating interactions of phonons with electrons or other energy carriers to advance fundamental science and device technologies beyond classical heat-transfer frameworks[15].

We have developed a nanoscale temperature-mapping approach based on tip-enhanced Raman spectroscopy[16–18] to measure temperature patterns generated under nanoscale heating excitation, thereby capturing the propagation of non-equilibrium phonon waves. Measurements are conducted in standard scanning tunnelling microscopy (STM) mode (Methods). The operating principles and a photograph of the experimental set-up are shown in Fig. 1a and b, respectively. A scanning probe with a nanoscale gold tip (Fig. 1c) is positioned near the sample surface, functioning as both a heat source and a temperature sensor. By applying an electrical current through the nanoscale tip, Joule heating is induced at the tunnelling junction, creating a nanoscale hot spot and generating temperature gradient profiles driven by heat flux. To visualize the temperature distribution, a single layer of 1-octadecanethiol molecules is uniformly coated on the sample surface through self-assembly driven by molecular bonding mechanisms[10,19]. Fundamentally, upon heating, the principle of thermal desorption selectively reduces the molecular density in regions with elevated temperatures, while molecules remain intact in cooler areas[10]. Consequently, characterization of the molecular surface coverage reveals the steady-state temperature distribution surrounding the nanoscale hot spot.

The nanoscale spatial resolution of temperature mapping is enabled by the operation principle of the tip-enhanced Raman technique[16–18]: when illuminated with an excitation laser (Fig. 1a), localized surface plasmons are excited at the tip apex, substantially enhancing the electromagnetic field in the cavity between the tip and the sample. This localized enhancement amplifies the Raman scattering signal from the molecules directly beneath the tip, thereby increasing detection sensitivity and enabling nanoscale spatial resolution approaching the tip apex size. The temperature sensitivity and nanoscale resolution of our experimental set-up were experimentally validated. As shown in Fig. 1d, tip-enhanced Raman spectra were collected from single-layer molecules on the sample surface at various temperatures. A characteristic Raman peak at ~1,338 cm^{-1}, corresponding to the C–C stretching and C–H bending modes in the molecules[20], gradually decreases in intensity with rising temperature due to thermal desorption, until the molecular layer is fully removed.

Comprehensive validation and quantitative analysis of the temperature-dependent experiments (Methods) further confirm the robustness, reproducibility and nanoscale resolution of the technique. Using this approach, we characterized temperature profiles generated by nanoscale heating. For example, measurements performed on a gold film and the corresponding two-dimensional Raman image (Fig. 1f) reveal a circular and continuous molecular pattern, characteristic of the diffusive heat conduction typically observed in common materials[4].

We investigated phonon focusing in boron arsenide (BAs), a recently discovered semiconductor[11,12,14,21–27]. As a cubic crystal, BAs exhibits an extraordinarily high thermal conductivity of 1,300 $W\,m^{-1}K^{-1}$, which is isotropic in all crystal directions and surpasses that of most common materials[11]. The synthesis and preparation of BAs single crystals are detailed in the Methods and our recent reports[11,12,21–23]. To verify the crystal quality, we used high-resolution transmission electron microscopy (TEM), which revealed atomically resolved lattice structures (Fig. 2a). The freshly cleaned BAs crystals were immersed in a 1 mM solution of octadecanethiol isomer in ethanol at room temperature for 24 h, forming a single layer of molecules on the sample surfaces. Subsequently, the BAs samples were characterized using nanoscale temperature heating and imaging, following the same approach as described above.

The measurement on BAs at room temperature is shown in Fig. 2d. Strikingly, it reveals ray-like features with six-branch symmetry on the BAs surface, which are consistently reproduced across multiple samples (Extended Data Fig. 3). This measurement indicates that heat flux travels from the central hot spot along the six high-symmetry directions with much greater intensity. This behaviour deviates notably from classical diffusive heat conduction, which would produce continuous temperature profiles, such as the circular pattern observed

https://doi.org/10.1038/s41567-026-03335-y

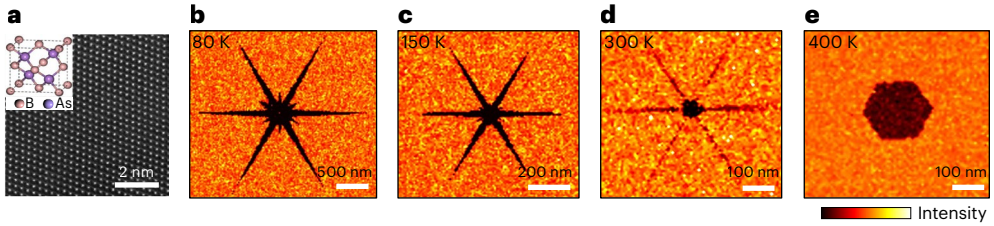

Fig. 2 | Experimental measurements of phonon focusing in cubic BAs crystals. **a**, High-resolution TEM image of a BAs single crystal. Inset: schematic of the zinc-blende face-centred cubic crystal structure with $F\bar{4}3m$ space group. **b**–**e**, Measured molecular profiles showing the evolution of phonon-focusing patterns at different temperatures: 80 K (**b**), 150 K (**c**), 300 K (**d**) and 400 K (**e**). The results represent temperature profiles measured on the (111) crystal surface. The colour bar denotes relative Raman intensity in arbitrary units. The colour scale increases from low (dark red) to high (yellow) Raman intensity.

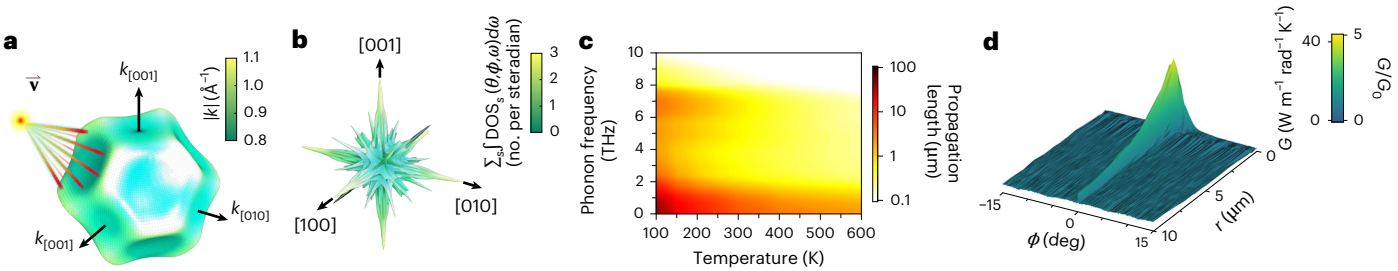

Fig. 3 | First-principles theory and analysis of phonon-focusing mechanisms. **a**, First-principles calculated three-dimensional phonon band structure of the BAs crystal. The plot shows an iso-frequency surface at 7.8 THz for the longitudinal phonon branch. **b**, First-principles calculated three-dimensional directional number of states, indicating the preferential transport directions and symmetry that give rise to phonon focusing. **c**, Calculated full-spectrum phonon propagation lengths as a function of phonon frequency and temperature, revealing the origin for room-temperature phonon focusing. **d**, Calculated heat conductance G under phonon focusing, shown as a ratio to the ballistic thermal conductance G_0, illustrating the spatial redistribution of thermal conductance and temperature, with peak conductance beyond the ballistic thermal transport limits due to phonon focusing effects. The results presented are for the (111) crystal surface. $G_0 = 8.68\ \mathrm{W\,m^{-1}\,rad^{-1}\,K^{-1}}$.

in Fig. 1f. The observed ray-like temperature patterns arise from the direction-preferred propagation of non-equilibrium phonon waves following hot excitation, leading to 'focused' phonon propagation in distinct principal directions—a phenomenon known as phonon focusing. The fundamental origin and theoretical analysis of phonon focusing are discussed below, but these measurements clearly demonstrate that phonon focusing can govern heat transport and produce exotic temperature profiles at room temperature.

We also conducted temperature-dependent measurements of the phonon-focusing patterns across a range of temperatures from 80 to 400 K. The experimental results, plotted in Fig. 2b–e, demonstrate the effects of temperature on the phonon-focusing patterns. Across all temperatures, the six-fold symmetry of the principal directions is maintained. Given that the surface plane of this BAs crystal is (111), the principal directions can be indexed along $[1\bar{1}0]$, $[\bar{1}10]$, $[10\bar{1}]$, $[\bar{1}01]$, $[01\bar{1}]$ and $[0\bar{1}1]$. However, the length of the focused phonon rays varies with temperature, from ~1.2 μm at 80 K, decreasing to ~350 nm at 150 K, and further to ~250 nm at 300 K, indicating stronger phonon scattering at higher temperatures. When the sample temperature exceeds 400 K, the measured patterns merge into a hexagonal structure (Fig. 2e), reflecting the persistence of six-fold principal symmetry from phonon focusing, while the temperature profile transitions towards the circular symmetry characteristic of classical heat conduction. Additionally, at low temperatures, secondary features were observed. At 80 K, secondary rays appeared along six minor symmetry directions: $[2\bar{1}\bar{1}]$, $[\bar{2}11]$, $[\bar{1}2\bar{1}]$, $[1\bar{2}1]$, $[\bar{1}\bar{1}2]$ and $[11\bar{2}]$. These secondary rays weaken at 150 K and become completely invisible at 300 K. This suggests that the minor focusing directions have phonon populations that are less concentrated than in the principal directions.

To understand the observed dynamics and underlying transport physics, we performed first-principles calculations[28–31]. Detailed descriptions of the first-principles theoretical methods are provided in the Methods and in recent publications by us and others[9–12,27–33]. Fundamentally, temperature is a collective result of phonon waves from all modes, characterized by wavevector $\mathbf{k}$ and phonon band index s (ref. 5). For each phonon mode, its heat flux $\mathbf{q}$, driven by a nanoscale excitation from the hot spot, can be quantified as the non-equilibrium deviation ($\delta n_{\mathbf{k}s}$) of the phonon density from the Bose–Einstein distribution, represented as

$$\mathbf{q}_{\mathbf{k}s} = \hbar\omega_{\mathbf{k}s}\mathbf{v}_{\mathbf{k}s}\delta n_{\mathbf{k}s} \tag{1}$$

where $\hbar$ is the reduced Planck constant, and $\omega_{\mathbf{k}s}$ and $\mathbf{v}_{\mathbf{k}s}$ represent the phonon frequency and group velocity, respectively. In reciprocal space, this equation indicates that the mode-dependent heat flux $\mathbf{q}_{\mathbf{k}s}$ is caused by a phonon wave propagating with velocity $\mathbf{v}_{\mathbf{k}s}$, while heat transport can be complicated by this mode dependence as the overall heat flux comprises integrated contributions of all phonon modes.

We performed first-principles calculations of the phonon band structure and found that, despite the isotropic thermal conductivity in real space caused by the uniform atomic arrangement in the cubic crystal lattice of BAs, anisotropy fundamentally exists in reciprocal space. As shown in Fig. 3a, the calculated iso-frequency surface highlights this anisotropy: the quasi-flat nature of the surfaces along specific high-symmetry directions allows a much higher probability for phonon waves to propagate in these symmetric directions, dictated by their direction-concentrated vector group velocities $\mathbf{v}_{\mathbf{k}s}$ (that is, normal to the surface), leading to the focusing effect.

In real space, heat flux is contributed by all phonon modes over the full Brillouin zone:

$$\begin{aligned} q(\theta,\phi,\mathbf{r}) &= \frac{1}{(2\pi)^3}\sum_s \int |\mathbf{q}_{\mathbf{k}s}|\delta\left(\Omega_{\theta,\phi} - \Omega_{\mathbf{k}s}\right)\mathrm{d}\mathbf{k} \\ &= \sum_s \int q_s(\theta,\phi,\mathbf{r},\omega)\,\mathrm{d}\omega \end{aligned} \tag{2}$$

https://doi.org/10.1038/s41567-026-03335-y

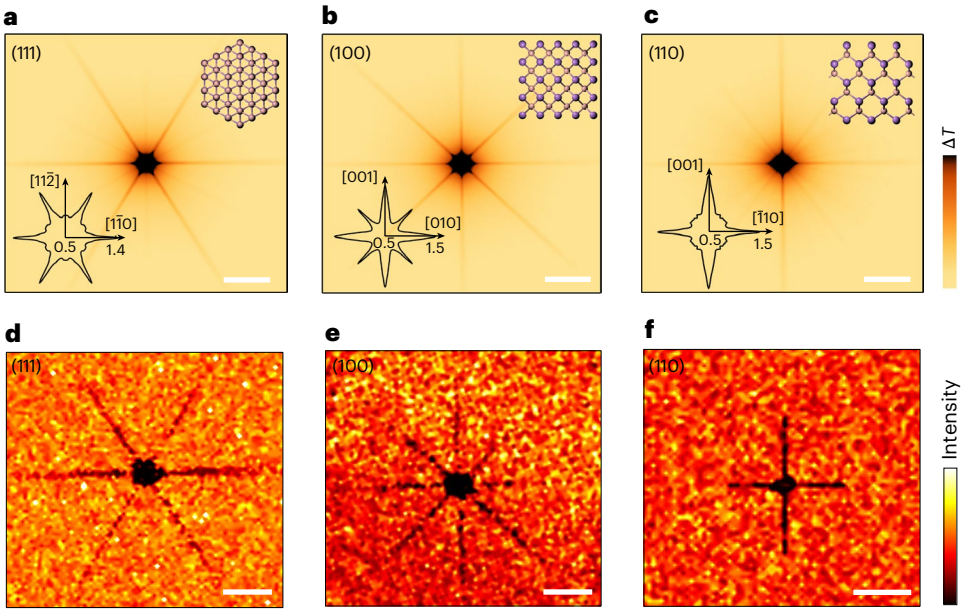

Fig. 4 | Theoretical predictions and experimental measurements of crystallographically dependent phonon-focusing symmetry at room temperature. **a**–**c**, Theoretically predicted phonon-focusing patterns from first-principles Boltzmann transport simulations along different crystal directions of BAs: (111) (**a**), (100) (**b**) and (110) (**c**). Insets: atomic planes viewed along various crystal orientations (right) and the corresponding directional number of states (no. per rad) (left). The colour scale denotes the normalized temperature rise, ΔT, increasing from low (yellow) to high (dark red). ΔT is normalized to the value at a point 30 nm from the heater centre along the horizontal axis. **d**–**f**, Experimental measurements of temperature profiles on BAs crystals with different crystallographic surface planes along (111) (**d**), (100) (**e**) and (110) (**f**). The measured phonon-focusing patterns, exhibiting six-fold, eight-fold and four-fold symmetries, respectively, show agreement with the theory predictions. The colour bar denotes relative Raman intensity in arbitrary units. The colour scale increases from low (dark red) to high (yellow) Raman intensity. Scale bars, 100 nm.

where $\Omega_{\theta,\phi}$ and $\Omega_{\mathbf{k}s}$ represent the solid angles in the (θ, ϕ) and $\mathbf{v}_{\mathbf{k}s}$ directions, respectively. $q_s(\theta, \phi, \mathbf{r}, \omega)$ is the spectral directional heat flux per unit frequency and solid angle:

$$q_s(\theta,\phi,\mathbf{r},\omega) = \hbar\omega v_s(\theta,\phi,\omega)\,\delta n_s(\theta,\phi,\mathbf{r},\omega)\,\mathrm{DOS}_s(\theta,\phi,\omega) \qquad (3)$$

Here, the directional density of states $\mathrm{DOS}_s(\theta, \phi, \omega)$ represents the number of phonon modes per unit frequency and solid angle, which weights the contribution to heat flux in each direction. As shown in Fig. 3b, the spectral integration of DOS_s is calculated as the directional number of states, highlighting high-symmetry directions where a large number of phonon modes travel, leading to phonon focusing along these crystal orientations. For example, in the crystal plane of (111), the major symmetry directions are determined by the theory to be $[1\bar{1}0]$, $[\bar{1}10]$, $[10\bar{1}]$, $[\bar{1}01]$, $[01\bar{1}]$ and $[0\bar{1}1]$, forming the six-fold principal symmetry that is consistent with the experimental measurement at room temperature in Fig. 2. In addition, the theory also predicted six minor symmetry directions, $[2\bar{1}\bar{1}]$, $[\bar{2}11]$, $[\bar{1}2\bar{1}]$, $[1\bar{2}1]$, $[\bar{1}\bar{1}2]$ and $[11\bar{2}]$, corresponding to the fine features measured at lower temperatures, as measured in Fig. 2b.

Based on the analysis, we attribute the fundamental origin of the observed temperature profiles of phonon focusing to the propagation-dependent non-equilibrium phonon density. The deviation $\delta n_{\mathbf{k}s}$ of all phonon modes collectively contributes to the temperature difference relative to the equilibrium background. Wave-like heat transport is characterized by phonon waves that experience minimal scattering and retain their orthogonal modes while propagating in distinct directions. Additionally, we find that, in the radial direction, the phonon waves propagate but gradually decay due to cumulatively increasing scattering. We quantify the damping of these phonon waves by defining a phonon propagation length, L_s:

$$\delta n_s(\theta,\phi,\mathbf{r},\omega) \sim \delta n_s(\theta,\phi,0,\omega)\, e^{-\frac{|\mathbf{r}|}{L_s(\theta,\phi,\omega)}} \qquad (4)$$

where the deviational phonon density decays exponentially, and the propagation length measures the distance the phonon wave can travel.

From first-principles theory, the spectral-dependent propagation length of BAs is calculated and presented as a function of temperature in Fig. 3c. Unlike acoustic or ultrasound waves—low-frequency mechanical vibrations (below gigahertz) that can propagate over long distances (more than centimetres)—temperature is primarily contributed by high-frequency thermal phonons (terahertz). As shown, the propagation length of the thermal phonons from high-frequency modes is much shorter than that of the low-frequency modes, explaining why observing phonon-focusing-induced temperature profiles has been challenging and limited to cryogenic temperatures[1–3]. In most materials, the spectral propagation length decreases dramatically at high frequency, but in BAs, even at room temperature, the propagation length persists up to micrometres across the phonon spectrum up to 8 THz, demonstrating the fundamental possibilities for the observed phonon focusing at room temperature.

To further elucidate the propagation dynamics of phonon waves, we used first-principles theory to quantitatively determine phonon transport by solving the full phonon spectrum-dependent Boltzmann equation[28–31]. All phonon properties, including dispersion, group velocities and scattering matrices, were determined using first-principles methods based on density functional theory (more details are provided in the Methods and the literature). To accurately describe the phonon scattering processes in the scenario of strong non-equilibrium, the scattering matrix is used to precisely determine the transitions between each pair of phonon modes, overcoming the limitations of the single-mode relaxation time approximation in such conditions[28–31].

Figure 3d presents the spatially dependent thermal conductance $G(r, \phi)$ of BAs under phonon focusing at room temperature. Two-dimensional mapping of thermal conductance, shown in a zoomed-in view near a principal symmetry direction ($\phi = 0$), reveals two key features. First, spreading along angular directions (ϕ), there

is substantial variation in conductance. The thermal conductance is substantially higher as a narrowly focused peak in the symmetry direction, but drops sharply at locations away from this direction. This angular distribution illustrates the physical origin of phonon focusing, which redistributes spatial heat conductance by directing phonon populations from nearby locations and more towards the symmetry directions, thereby substantially enhancing thermal conductance in these directions. For a quantitative comparison, we plotted G as a ratio relative to the ballistic thermal conductance (G_0), which represents the scenario where all phonon modes undergo ballistic transport without scattering losses and uniformly radiate in all directions (Methods). G_0 is typically considered the upper limit of thermal conductance in solids, or the radiation limit. It is interesting to note that the phonon-focusing effect redistributes the conductance at the symmetry line, forming a peak conductance to exceed the ballistic thermal conductance, that is, $G/G_0 > 1$. Second, in the radial direction (r), phonon focusing, characterized by directionally enhanced thermal conductance, decays with r but remains pronounced at room temperature. The orders-of-magnitude longer propagation lengths of a broad spectrum of phonon modes in BAs explain the unusual observation of such exotic temperature phenomena at room temperature.

Importantly, first-principles theoretical calculations further predict unique transport symmetries that depend on crystal orientation, revealing distinct propagation characteristics of phonon waves across various crystal planes of BAs. As shown in Fig. 4a–c respectively, distinct six-fold, eight-fold and four-fold focusing patterns are theoretically calculated for the (111), (100) and (110) crystal planes. For the theory, these intrinsic variations in phonon-focusing patterns originate from the lattice symmetries in each preferred direction (Fig. 4a–c, top right insets), which result in the corresponding directional number of states in the surface plane (Fig. 4a–c, bottom left insets). For instance, the lattice structure of the (111) surface exhibits six mirror symmetries due to its triangular atomic arrangement, where each atom is surrounded by six equidistant neighbours, forming a repeating pattern of equilateral triangles. The equilateral triangle has three symmetry lines passing through its vertices and three more along its edges, resulting in a total of six mirror planes. Each symmetry line creates two equivalent paths in opposite directions along the mirror plane. The three symmetry lines passing through the triangle vertices lead to the formation of six principal peaks in $\mathrm{DOS}_s(\theta, \phi, \omega)$, while the other three symmetry lines along the triangle edges correspond to the six minor peaks.

To test these theoretical predictions, we performed additional experiments along different crystal orientations. We prepared different BAs samples with (111), (100) and (110) surfaces and measured their heat-flux-driven temperature profiles, as shown in Fig. 4d–f. The measurements reveal distinct six-fold, eight-fold and four-fold phonon-focusing patterns, respectively, highlighting the inherent influence of in-plane crystal symmetry and showing close agreement with the theoretical calculations in Fig. 4a–c. For instance, the eight-fold phonon-focusing pattern on the (100) surface arises from the symmetric preferential travelling directions along [011], [01$\bar{1}$], [0$\bar{1}$1], [0$\bar{1}\bar{1}$], [001], [00$\bar{1}$], [010] and [0$\bar{1}$0]. In contrast, the four-fold phonon-focusing feature on the (110) surface arises from the inequivalent horizontal and vertical directions, [00$\bar{1}$]/[001] and [1$\bar{1}$0]/[$\bar{1}$10]. These results confirm that the symmetry and propagation dynamics of phonon focusing are governed by crystallographic orientation, reciprocal-space anisotropy and non-equilibrium phonon propagation, and that the resulting temperature patterns can be quantitatively predicted from the underlying transport physics. Together, they provide fundamental insights into unconventional, wave-governed heat transport and highlight the potential of extreme thermal materials[9–14] to access exotic transport regimes rooted in the quantum nature of phonons at room temperature.

Our findings show that phonon focusing can persist at and above room temperature, establishing a new regime of heat transport in which non-equilibrium phonons retain pronounced wave-like and symmetry-governed behaviour under ambient conditions. These exotic, ray-like temperature profiles concentrated along symmetry directions are markedly distinct from those of classical heat transfer. More broadly, the results indicate that wave-governed exotic and quantum transport phenomena, long thought to be confined to cryogenic settings, can become experimentally accessible at technologically relevant temperatures in advanced materials. Looking ahead, the discovery of ambient phonon wave dynamics, together with the ability to directionally control heat flow and precisely tailor phonon coupling to other energy carriers, could open new frontiers beyond classical thermal-management frameworks[14], enabling phononic metastructures and new device concepts for thermal, electronic and quantum technologies.

Online content

Any methods, additional references, Nature Portfolio reporting summaries, source data, extended data, supplementary information, acknowledgements, peer review information; details of author contributions and competing interests; and statements of data and code availability are available at https://doi.org/10.1038/s41567-026-03335-y.

References

1. Taylor, B., Maris, H. J. & Elbaum, C. Phonon focusing in solids. *Phys. Rev. Lett.* **23**, 416–419 (1969).
2. Northrop, G. A. & Wolfe, J. P. Ballistic phonon imaging in solids—a new look at phonon focusing. *Phys. Rev. Lett.* **43**, 1424–1427 (1979).
3. Hensel, J. C. & Dynes, R. C. Observation of singular behavior in the focusing of ballistic phonons in Ge. *Phys. Rev. Lett.* **43**, 1033–1036 (1979).
4. Bergman, T. L., Lavine, A. S., Incropera, F. P. & Dewitt, D. P. *Fundamentals of Heat and Mass Transfer* 7th edn (Wiley, 2011).
5. Ziman, J. M. *Electrons and Phonons: The Theory of Transport Phenomena in Solids* (Oxford Univ. Press, 1960).
6. Kuleyev, I. G., Kuleyev, I. I., Bakharev, S. M. & Ustinov, V. V. *Phonon Focusing and Phonon Transport: In Single-Crystal Nanostructures* (De Gruyter, 2020).
7. Bron, W. E. *Nonequilibrium Phonon Dynamics* (Springer, 1985).
8. Wolfe, J. P. *Imaging Phonons: Acoustic Wave Propagation in Solids* (Cambridge Univ. Press, 1998).
9. Li, S. et al. Metallic θ-phase tantalum nitride has a thermal conductivity triple that of copper. *Science* **391**, 707–711 (2026).
10. Li, M. et al. Electrically gated molecular thermal switch. *Science* **382**, 585–589 (2023).
11. Kang, J. S., Li, M., Wu, H., Nguyen, H. & Hu, Y. Experimental observation of high thermal conductivity in boron arsenide. *Science* **361**, 575–578 (2018).
12. Li, S. et al. Anomalous thermal transport under high pressure in boron arsenide. *Nature* **612**, 459–464 (2022).
13. Cui, Y., Li, M. & Hu, Y. Emerging interface materials for electronics thermal management: experiments, modeling, and new opportunities. *J. Mater. Chem. C* **8**, 10568–10586 (2020).
14. Li, M. et al. Advancing thermal management technology for power semiconductors through materials and interface engineering. *Acc. Mater. Res.* **6**, 563–576 (2025).
15. Su, C. et al. Nonclassical heat transfer and recent progress. *ASME J. Heat Mass Transf.* **147**, 032502 (2025).
16. Zrimsek, A. B. et al. Single-molecule chemistry with surface- and tip-enhanced Raman spectroscopy. *Chem. Rev.* **117**, 7583–7613 (2017).
17. Wang, X. et al. Tip-enhanced Raman spectroscopy for surfaces and interfaces. *Chem. Soc. Rev.* **46**, 4020–4041 (2017).
18. Deckert-Gaudig, T., Taguchi, A., Kawata, S. & Deckert, V. Tip-enhanced Raman spectroscopy—from early developments to recent advances. *Chem. Soc. Rev.* **46**, 4077–4110 (2017).

19. Sheen, C. W., Shi, J. X., Maartensson, J., Parikh, A. N. & Allara, D. L. A new class of organized self-assembled monolayers: alkane thiols on gallium arsenide(100). *J. Am. Chem. Soc.* **114**, 1514–1515 (1992).
20. Kim, K. & Lee, H. S. Effect of Ag and Au nanoparticles on the SERS of 4-aminobenzenethiol assembled on powdered copper. *J. Phys. Chem. B* **109**, 18929–18934 (2005).
21. Kang, J. S. et al. Integration of boron arsenide cooling substrates into gallium nitride devices. *Nat. Electron.* **4**, 416–423 (2021).
22. Cui, Y., Qin, Z., Wu, H., Li, M. & Hu, Y. Flexible thermal interface based on self-assembled boron arsenide for high-performance thermal management. *Nat. Commun.* **12**, 1284 (2021).
23. Kang, J. S., Li, M., Wu, H., Nguyen, H. & Hu, Y. Basic physical properties of cubic boron arsenide. *Appl. Phys. Lett.* **115**, 122103 (2019).
24. Dames, C. Ultrahigh thermal conductivity confirmed in boron arsenide. *Science* **361**, 549–550 (2018).
25. Li, S. et al. High thermal conductivity in cubic boron arsenide crystals. *Science* **361**, 579–581 (2018).
26. Tian, F. et al. Unusual high thermal conductivity in boron arsenide bulk crystals. *Science* **361**, 582–585 (2018).
27. Lindsay, L., Broido, D. A. & Reinecke, T. L. First-principles determination of ultrahigh thermal conductivity of boron arsenide: a competitor for diamond? *Phys. Rev. Lett.* **111**, 025901 (2013).
28. Fan, H., Wu, H., Lindsay, L. & Hu, Y. Ab initio investigation of single-layer high thermal conductivity boron compounds. *Phys. Rev. B* **100**, 085420 (2019).
29. Wu, H., Fan, H. & Hu, Y. Ab initio determination of ultrahigh thermal conductivity in ternary compounds. *Phys. Rev. B* **103**, L041203 (2021).
30. Wu, H., Qin, Z., Li, S., Lindsay, L. & Hu, Y. Nonperturbative determination of isotope-induced anomalous vibrational physics. *Phys. Rev. B* **108**, L140302 (2023).
31. Wu, H. & Hu, Y. Ab initio investigations on hydrodynamic phonon transport: from diffusion to convection. *Int. J. Heat Mass Transf.* **220**, 124988 (2024).
32. Garg, J., Bonini, N., Kozinsky, B. & Marzari, N. Role of disorder and anharmonicity in the thermal conductivity of silicon-germanium alloys: a first-principles study. *Phys. Rev. Lett.* **106**, 045901 (2011).
33. Feng, T., Lindsay, L. & Ruan, X. Four-phonon scattering significantly reduces intrinsic thermal conductivity of solids. *Phys. Rev. B* **96**, 161201 (2017).

Methods

Sample preparation and characterizations

High-quality cubic BAs crystals were synthesized by means of the chemical vapour transport method. The reaction sources were introduced into a quartz tube after grinding high-purity boron and arsenic powders (99.9999%, Alfa Aesar) using a mortar and pestle in a stoichiometric ratio of 1:2. After evacuating and flame-sealing the tube under high vacuum (10^{-5} torr), the tube was placed into a customized three-zone reaction furnace with a 1,083-K hot zone, 1,058-K centre zone and 1,033-K cold zone. Further details of the chemical synthesis of BAs can be found in our recent reports[11,12,21–23].

The as-synthesized crystals were immediately placed into a capped vial with a 1 mM solution of 1-octadecanethiol isomer in ethanol (Sigma-Aldrich) after careful cleaning with hydrochloric acid, acetone and ethanol, then left at room temperature (~25 °C) for 24 h. The sample was then removed, rinsed with ethanol and dried with nitrogen. Further details on the preparation of self-assembled monolayer molecules can be found in the literature reports from us and others[10,19].

The sample for TEM imaging of the BAs crystal structure was prepared using a focused ion beam (FIB) apparatus (Nova 600, FEI). Initially, the sample was cut by the FIB into a miniature slab with dimensions of 8 µm (width), 8 µm (height) and 2 µm (thickness). A nanomanipulator was used to transfer the slab onto a TEM sample holder (PELCO FIB Lift-Out, Ted Pella). To ensure the sample was thin enough (<100 nm) for effective electron-beam penetration during TEM imaging, it was subsequently milled with the FIB and further refined by nanomilling (model 1040 NanoMill, Fischione), gradually lowering the voltage. Once the milling process was complete, the sample was transferred to an aberration-corrected scanning TEM instrument (Grand ARM, JEOL) for imaging.

Nanoscale heating and tip-enhanced Raman measurements

Localized nanoscale heating was achieved with a tunnelling current across the junction between a nanoscale gold tip and the sample surface, following a standard scanning tunnelling microscope (STM) procedure. The gold tip was prepared by electrochemical etching in a hydrochloric acid:ethanol (1:1) solution under an applied voltage of 2.4 V (ref. 34).

For nanoscale heating, the tip was approached to the sample surface using a scanning probe microscope (Bruker Innova-IRIS) under a constant voltage of 1 V and with a target tunnelling current of 1 nA. Once a stable tunnelling current was established, it was gradually increased to a higher level (up to 1–10 mA) and maintained for several seconds to induce localized heating.

For Raman mapping, a low current (~1 nA) was used to enable non-invasive measurements. A 633-nm laser (0.1 mW power) was focused onto the gold tip using a ×50 long working distance objective lens (Mitutoyo SLWD ×50) from the side. Raman-scattered photons were collected and analysed using a Renishaw inVia Raman spectrometer. Once optimal alignment was achieved, the Raman signal was maximized.

The mapping experiment was performed by scanning the sample with a piezoelectric stage over an area of $1 \times 1\ \mu m^2$. The resulting temperature distribution was derived from the integrated Raman intensity within the 1,325–1,355 cm^{-1} range. Image processing and data analysis were conducted using MATLAB (MathWorks).

Characterizations of Raman spectra

Temperature-dependent Raman spectroscopy was performed across multiple samples and over an extended period. As shown in Extended Data Fig. 1, temperature-dependent Raman data from ten different samples were recorded and plotted together to demonstrate consistency and reproducibility. In addition, as shown in Extended Data Fig. 2, we conducted a long-term stability test to evaluate the robustness of the molecular layers. Raman intensities were monitored over 30 days, and no appreciable change was observed.

Phonon focusing verified across multiple samples and quantitative analysis

To evaluate the reproducibility of phonon focusing, measurements were performed on multiple samples. As shown in Extended Data Fig. 3, the phonon-focusing patterns measured from different samples exhibit consistent and repeatable results. In addition, the high-resolution Raman mapping enabled quantitative analysis. Specifically, the Raman intensity was extracted as a function of both rotation angle and radial distance, as shown in Extended Data Fig. 3d,e.

Nanoscale spatial resolution of the measurements

The spatial resolution in our set-up is primarily determined by three factors: the STM piezoelectric positioning system and settings, the tip apex size, and the signal-to-noise ratio of the Raman measurement. To validate the spatial resolution, we performed high-resolution scans across fine temperature distribution profiles, and the pixel-resolved experimental data were analysed. As shown in Extended Data Fig. 4a, two-dimensional mapping measurements reveal nanoscale features. Additionally, position-dependent experimental data measured along different locations are plotted in Extended Data Fig. 4b. These results confirm the system's capability for nanoscale spatial resolution.

Density functional theory calculations of phonon properties of materials

We applied first-principles theoretical approaches based on density functional theory to calculate the phonon properties[9–12,21,27,28,30–33,35–42]. The phonon dispersion, which is the relationship between phonon frequency and phonon wave vector, is determined by diagonalizing the dynamical matrix. The dynamical matrix is determined by second-order interatomic force constants (IFCs), which are the second derivatives of the potential energy with respect to the atomic displacements. The group velocity is determined by the derivative of the phonon frequency with respect to the wave vector. The phonon mean free path $\Lambda_{\mathbf{k}s}$ is determined by $\Lambda_{\mathbf{k}s} = |\mathbf{v}_{\mathbf{k}s}|\,\tau_{\mathbf{k}s}$, where $\mathbf{v}_{\mathbf{k}s}$ and $\tau_{\mathbf{k}s}$ are the phonon group velocity and the relaxation time of the phonon mode with wave vector $\mathbf{k}$ and branch index s, respectively. The phonon relaxation time is calculated by Fermi's golden rule[43], treating the anharmonicity and isotopes as perturbations to the harmonic lattice dynamics. The third- and fourth-order IFCs are used to determine the three- and four-phonon anharmonic scatterings, respectively. The IFCs are determined using the finite displacement method[12,29,30]. In this method, an irreducible displacement set is generated on a 216-atom supercell. For each displacement configuration, the forces acting on the atoms are calculated by density functional theory using Quantum ESPRESSO[44,45], which determines the displacement–force sets. The IFCs are extracted by fitting the displacement–force sets using ALAMODE[46]. Up to the fifth and second nearest-neighbouring atoms are considered for the third- and fourth-order IFCs, respectively.

In density functional theory calculations, we use PZ pseudopotentials (B.pz-n-kjpaw_psl.0.1.UPF and As.pz-n-kjpaw_psl.0.2.UPF from http://www.quantum-espresso.org) under the local density approximation and the projector-augmented wave approach. The Monkhorst–Pack grid for the 216-atom supercell is $2 \times 2 \times 2$. The kinetic energy cutoff for electronic wavefunctions is 120 Ry. The convergence threshold for self-consistency is 10^{-11}. The directional number of states and the relaxation time are calculated on $200 \times 200 \times 200$ and $18 \times 18 \times 18$ Monkhorst–Pack grids, respectively.

Ballistic heat conductance

Ballistic thermal transport represents a regime where phonon scattering losses are absent[47,48]. The ballistic heat conductance G_0 is calculated based on the experimental geometry in this study, where phonons are

emitted uniformly in all directions from a circular heater of radius R, and the conductance per unit angle and unit length can be expressed as[49]

$$G_0 = R\sum_s \int_{\mathrm{BZ}} \hbar\omega_{\mathbf{k}s} |\mathbf{v}_{\mathbf{k}s,\parallel}| \frac{\partial n^0_{\mathbf{k}s}}{\partial T} \mathrm{d}\mathbf{k} \quad (5)$$

where $\omega_{\mathbf{k}s}$, $n^0_{\mathbf{k}s}$ and $\mathbf{v}_{\mathbf{k}s,\parallel}$ are the phonon frequency, Bose–Einstein distribution and in-plane component of group velocity for phonon mode $\mathbf{k}s$, respectively.

First-principles Boltzmann transport simulations of phonon focusing

Details of the first-principles Boltzmann transport simulations of phonon transport can be found in recent publications[9–12,21,28–31]. Phonon-transport behaviour and dynamics were determined from first-principles calculations using a variance-reduced Monte Carlo algorithm building on our recent developments[21,31,48], to solve the three-dimensional deviational Boltzmann transport equation with the full phonon scattering matrix:

$$\frac{\partial \delta n_{\mathbf{k}s}}{\partial t} + \mathbf{v}_{\mathbf{k}s} \cdot \nabla \delta n_{\mathbf{k}s} = \sum_{\mathbf{k}'s'} A_{\mathbf{k}s,\mathbf{k}'s'} \delta n_{\mathbf{k}'s'} \quad (6)$$

where $\delta n_{\mathbf{k}s} = n_{\mathbf{k}s} - n^0_{\mathbf{k}s}$ is the deviation of the non-equilibrium phonon distribution ($n_{\mathbf{k}s}$) from the equilibrium Bose–Einstein distribution ($n^0_{\mathbf{k}s}$). $A_{\mathbf{k}s,\mathbf{k}'s'}$ is the scattering matrix that quantifies the transition rates from $\mathbf{k}'s'$ to $\mathbf{k}s$. Conventionally, the single-mode relaxation time is assigned to each phonon mode to describe phonon scatterings, assuming that the background phonons are under equilibrium. However, for high-thermal-conductivity materials with weak phonon scatterings, such as BAs, this approximation loses accuracy due to there being insufficient phonon scattering to maintain local thermal equilibrium. To accurately capture the phonon dynamics in BAs, the scattering matrix is used to finely determine the transitions between each pair of phonon modes. The scattering matrix is derived by quantum perturbation theory, considering three- and four-phonon anharmonic scatterings and isotope scatterings[9,12,29]. The scattering matrix is derived on $18 \times 18 \times 18$ Monkhorst–Pack grids for $\mathbf{k}$ points, with IFCs determined by a first-principles approach based on density functional theory. We initialize the phonons with radial positions determined by Gaussian distribution, with a heater diameter of 5 nm. The phonon dynamics are then simulated to determine the evolution of temperature and heat flux fields[31]. Time integration is employed to obtain the results at steady state. To compute the directional thermal conductance, the heater temperature and the directional heat flux are sampled, with the latter taken at various radial positions using a mesh of 720,000 grids on the azimuthal angle. The spatial distribution of temperature is sampled using a mesh of 360 grids on the azimuthal angle and a radial step of 10 nm.

Further analysis was conducted to evaluate the effects of various conditions on phonon transport. The spatial distribution of heat conductance under phonon focusing, obtained from first-principles Boltzmann transport simulations, is shown in Fig. 3d. Using the calibrated temperature–Raman intensity relationship, the temperature distributions corresponding to the experimentally observed phonon-focusing patterns were reconstructed, and are plotted with simulation results in Extended Data Fig. 5. To assess surface effects, both specular and diffuse boundary scattering conditions were examined in the transport modelling, as presented in Extended Data Fig. 6. The influence of crystal defects on phonon focusing was also quantitatively evaluated and is shown in Extended Data Fig. 7. To examine the uncertainty of the calculated temperature, we performed a convergence test, as shown in Extended Data Fig. 8. The converged heater temperatures are plotted as a function of the number of sampling particles, with error bars representing the standard deviation from 20 independent simulation runs. The results show that the heater temperature converges rapidly, with the uncertainty falling below 0.09 K when the number of sampling particles exceeds 10^8. This confirms that numerical uncertainties in the theoretical results are negligibly small relative to the observed transport phenomena.

Phonon properties of BAs compared with other materials

As shown in Extended Data Fig. 9, the spectral phonon propagation lengths were calculated using first-principles theory. The results for BAs show long propagation lengths across nearly all phonon modes at room temperature. Additionally, Extended Data Fig. 10 presents the mode-dependent phonon scattering rates of BAs alongside those of diamond and cubic boron nitride, further illustrating the ultraweak phonon scattering behaviour of BAs.

Data availability

All data are available from the corresponding author upon reasonable request.

Code availability

The code that supports the findings of this study is available from the corresponding author upon reasonable request.

References

34. Ren, B., Picardi, G. & Pettinger, B. Preparation of gold tips suitable for tip-enhanced Raman spectroscopy and light emission by electrochemical etching. *Rev. Sci. Instrum.* **75**, 837–841 (2004).
35. Broido, D. A., Malorny, M., Birner, G., Mingo, N. & Stewart, D. A. Intrinsic lattice thermal conductivity of semiconductors from first principles. *Appl. Phys. Lett.* **91**, 231922 (2007).
36. Ward, A., Broido, D. A., Stewart, D. A. & Deinzer, G. Ab initio theory of the lattice thermal conductivity in diamond. *Phys. Rev. B* **80**, 125203 (2009).
37. Esfarjani, K., Chen, G. & Stokes, H. T. Heat transport in silicon from first-principles calculations. *Phys. Rev. B* **84**, 85204 (2011).
38. Li, W. et al. Thermal conductivity of diamond nanowires from first principles. *Phys. Rev. B* **85**, 195436 (2012).
39. Fugallo, G. et al. Thermal conductivity of graphene and graphite: collective excitations and mean free paths. *Nano Lett.* **14**, 6109–6114 (2014).
40. Landon, C. D. & Hadjiconstantinou, N. G. Deviational simulation of phonon transport in graphene ribbons with ab initio scattering. *J. Appl. Phys.* **116**, 163502 (2014).
41. Kang, J. S., Wu, H., Li, M. & Hu, Y. Intrinsic low thermal conductivity and phonon renormalization due to strong anharmonicity of single-crystal tin selenide. *Nano Lett.* **19**, 4941–4948 (2019).
42. Qin, Z. et al. Moiré pattern controlled phonon polarizer based on twisted graphene. *Adv. Mater.* **36**, 2312176 (2024).
43. Srivastava, G. P. *The Physics of Phonons* (CRC Press, 1990).
44. Giannozzi, P. et al. QUANTUM ESPRESSO: a modular and open-source software project for quantum simulations of materials. *J. Phys. Condens. Matter* **21**, 395502 (2009).
45. Giannozzi, P. et al. Advanced capabilities for materials modelling with Quantum ESPRESSO. *J. Phys. Condens. Matter* **29**, 465901 (2017).
46. Tadano, T., Gohda, Y. & Tsuneyuki, S. Anharmonic force constants extracted from first-principles molecular dynamics: applications to heat transfer simulations. *J. Phys. Condens. Matter* **26**, 225402 (2014).
47. Hu, Y., Zeng, L., Minnich, A. J., Dresselhaus, M. S. & Chen, G. Spectral mapping of thermal conductivity through nanoscale ballistic transport. *Nat. Nanotechnol.* **10**, 701–706 (2015).
48. Kang, J. S., Wu, H. & Hu, Y. Thermal properties and phonon spectral characterization of synthetic boron phosphide for high thermal conductivity applications. *Nano Lett.* **17**, 7507–7514 (2017).
49. Chen, G. *Nanoscale Energy Transport and Conversion: A Parallel Treatment of Electrons, Molecules, Phonons, and Photons* (Oxford Univ. Press, 2005).

Acknowledgements
We thank S. Prikhodko, A. Krayev and J. Mann for technical assistance and helpful discussions. We thank the technical staff at the UCLA Nanolab and the California NanoSystems Institute for their support.

Author contributions
Y.H. conceived the project and directed the research. M.L., Z.Q. and H.D.N. performed the experiments. H.W. and C.S. performed the first-principles calculations and phonon Boltzmann transport equation simulations. All authors discussed the results and commented on the paper.

Funding
Y.H. acknowledges partial support from the US Department of Energy (DOE), Office of Science, Office of Basic Energy Sciences and Office of Fusion Energy Sciences, as part of Co-design and Heterogeneous Integration in Microelectronics for Extreme Environments, a Microelectronics Science Research Center (MSRC); from the National Science Foundation (NSF) under DMR-1753393; from a NIGMS Research Award (R35GM147391); and from a gift fund provided by Parag and Falguni Patel in support of our research. Y.H. also acknowledges support from the computational and storage services associated with the Hoffman 2 Shared Cluster provided by UCLA Institute for Digital Research and Education's Research Technology Group, and Bridges-2 at Pittsburgh Supercomputing Center through allocation no. DMR180111 from the Advanced Cyberinfrastructure Coordination Ecosystem: Services & Support (ACCESS) programme supported by NSF grants 2138259, 2138286, 2138307, 2137603 and 2138296.

Competing interests
The authors declare no competing interests.

Additional information
Extended data is available for this paper at https://doi.org/10.1038/s41567-026-03335-y.

Supplementary information The online version contains supplementary material available at https://doi.org/10.1038/s41567-026-03335-y.

Correspondence and requests for materials should be addressed to Yongjie Hu.

Peer review information *Nature Physics* thanks Fei Tian and the other, anonymous, reviewer(s) for their contribution to the peer review of this work.

https://doi.org/10.1038/s41567-026-03335-y

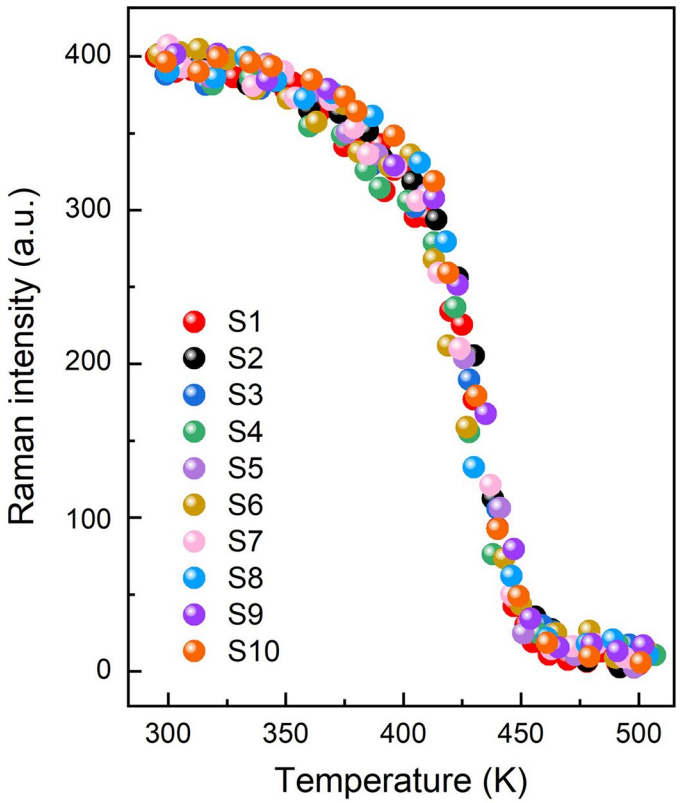

Extended Data Fig. 1 | Reproducibility of temperature-dependent Raman calibration. Raman intensity measured as a function of temperature for ten independent samples, showing consistent temperature-dependent Raman response.

https://doi.org/10.1038/s41567-026-03335-y

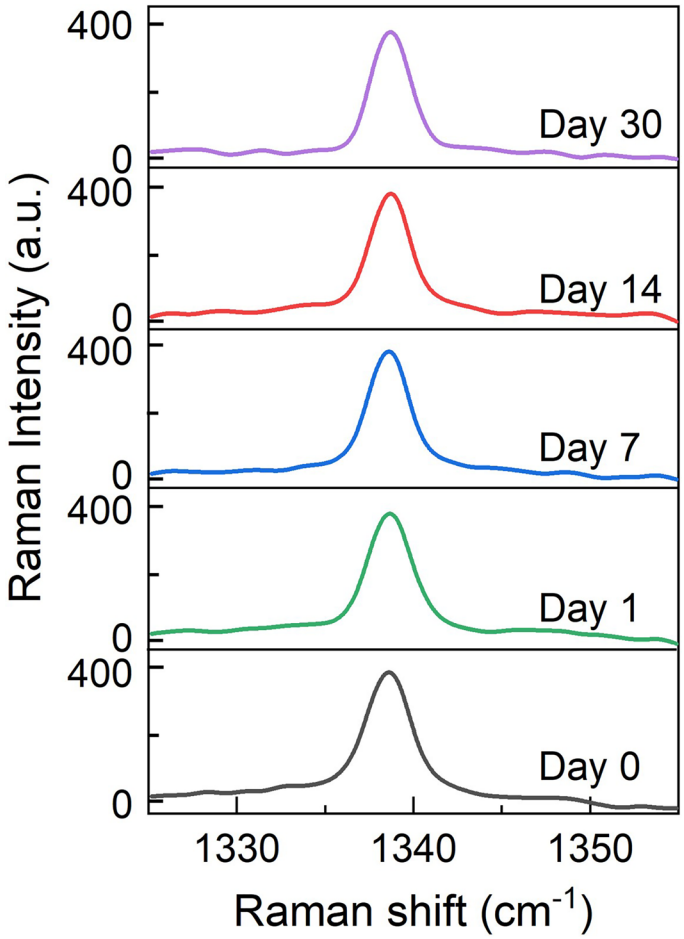

Extended Data Fig. 2 | Long-term stability test of the samples. Raman spectra collected over 30 days show negligible changes in the characteristic Raman peak, confirming sample stability for the experiments.

https://doi.org/10.1038/s41567-026-03335-y

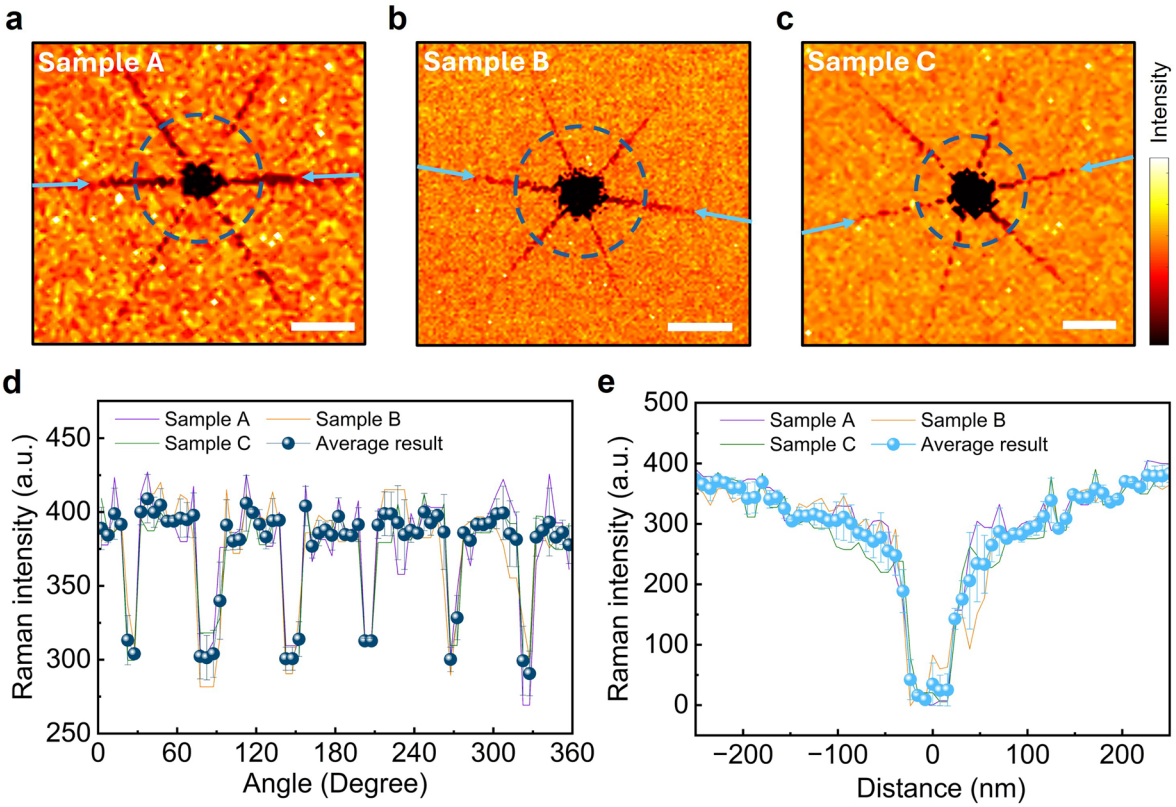

Extended Data Fig. 3 | Experimental measurements on different BAs samples. **a-c**, Measurement results of phonon focusing for Samples A, B, and C, respectively. Scale bar: 100 nm. Crystal surfaces are oriented along (111). **d**, Experimental data collected along a circle with a 100 nm radius from the heating center (indicated by circles in a–c), with data from different samples plotted together. **e**, Experimental data collected along a phonon focusing ray (indicated by arrows in **a-c**), with data from different samples plotted together. Error bars represent the standard deviation across the three samples.

https://doi.org/10.1038/s41567-026-03335-y

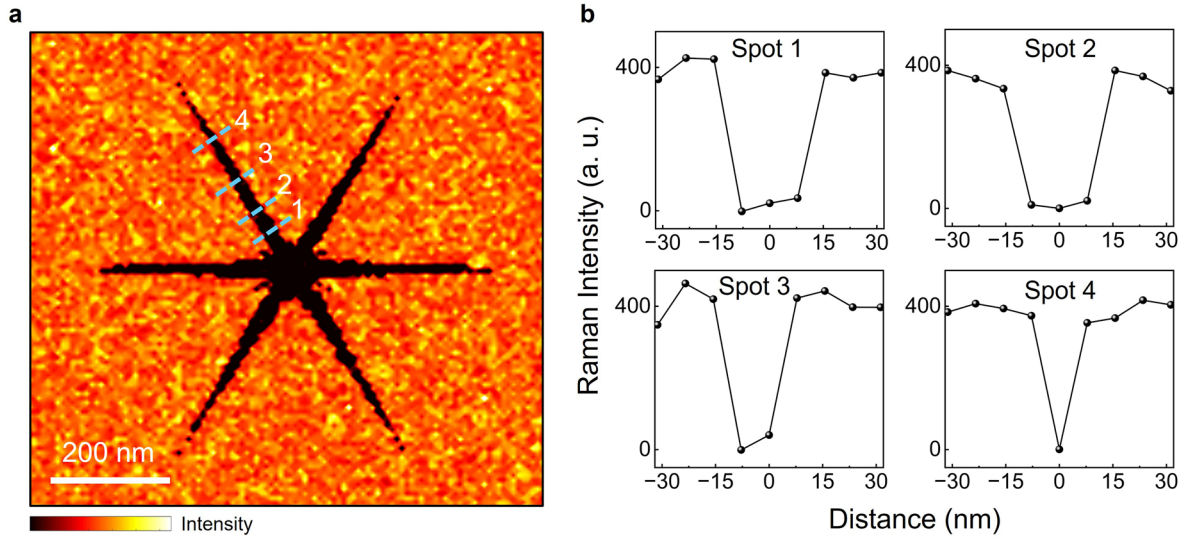

Extended Data Fig. 4 | Experimental measurements demonstrating nanoscale resolution. a, Two-dimensional temperature imaging reveals nanoscale features, exemplified by the dashed line. **b**, One-dimensional profiles measured at different locations, showing nanoscale detection resolution.

https://doi.org/10.1038/s41567-026-03335-y

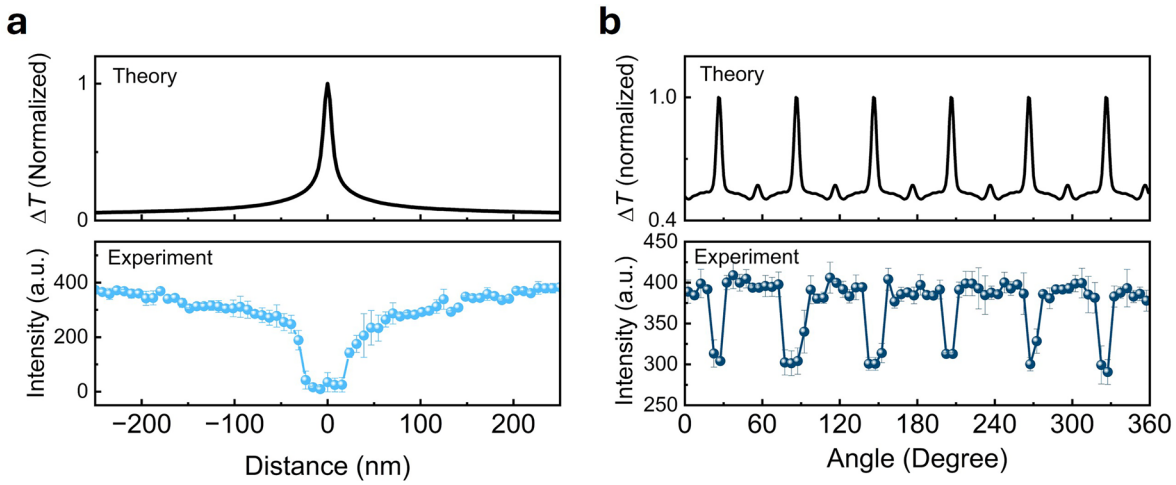

Extended Data Fig. 5 | Position-dependent data from experimental measurements and theoretical calculations. a, Data extracted along a phonon focusing ray. **b**, Data extracted along a circular path centred on the hot spot. Error bars represent the standard deviation across the three samples.

https://doi.org/10.1038/s41567-026-03335-y

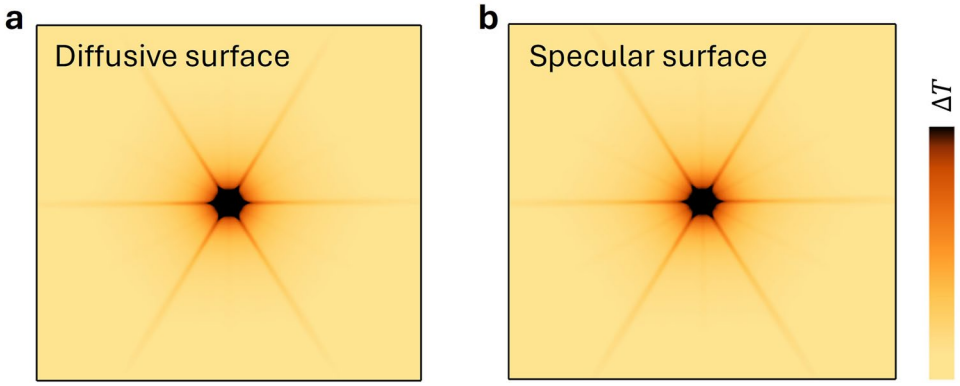

Extended Data Fig. 6 | Simulated phonon focusing under different surface boundary conditions. a, Diffuse boundary scattering. **b**, Specular boundary scattering. The colour scale denotes temperature normalized to the value at a point 30 nm from the heater center along the horizontal axis. The mapped region spans 600 nm × 600 nm.

https://doi.org/10.1038/s41567-026-03335-y

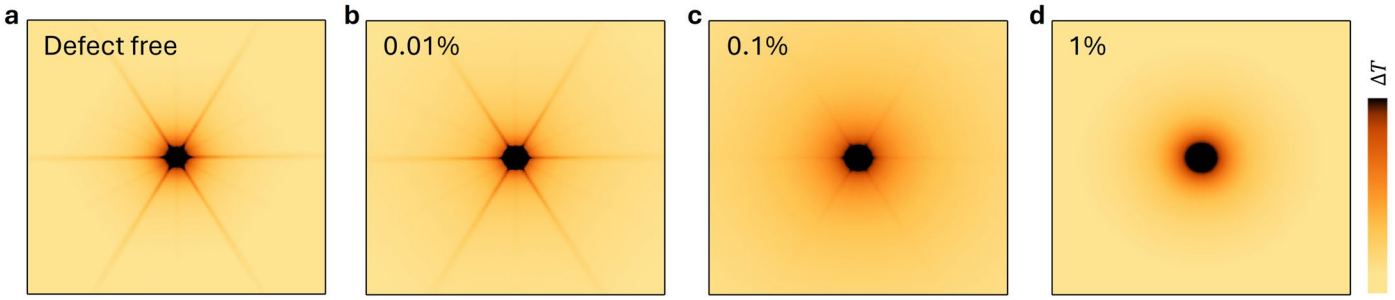

Extended Data Fig. 7 | Phonon transport evaluated as a function of varying vacancy defect concentrations. a–**d**, The colour scale denotes temperature normalized to the value at a point 30 nm from the heater center along the horizontal axis. The mapped region spans 600 nm × 600 nm.

https://doi.org/10.1038/s41567-026-03335-y

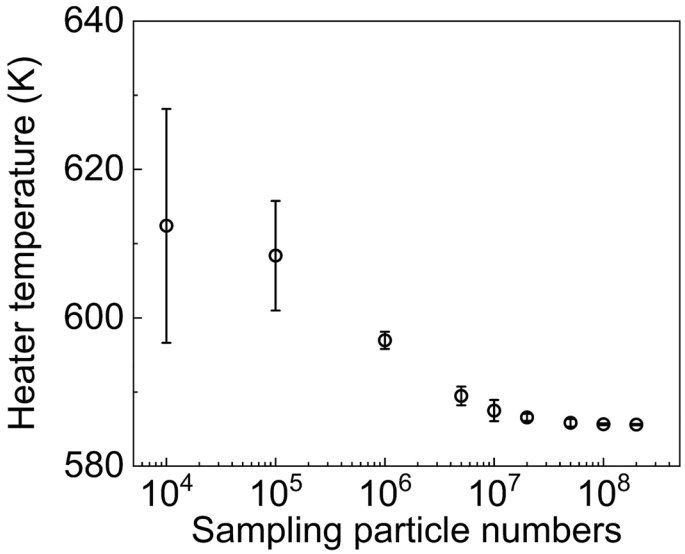

Extended Data Fig. 8 | Convergence test for uncertainty quantification. Heater temperature is evaluated as a function of the number of sampling particles. Error bars represent standard deviation over 20 independent simulation runs; center values indicate the mean. A convergence threshold of less than 0.05% in the temperature rise relative to the background temperature is applied throughout all calculations to ensure high accuracy.

https://doi.org/10.1038/s41567-026-03335-y

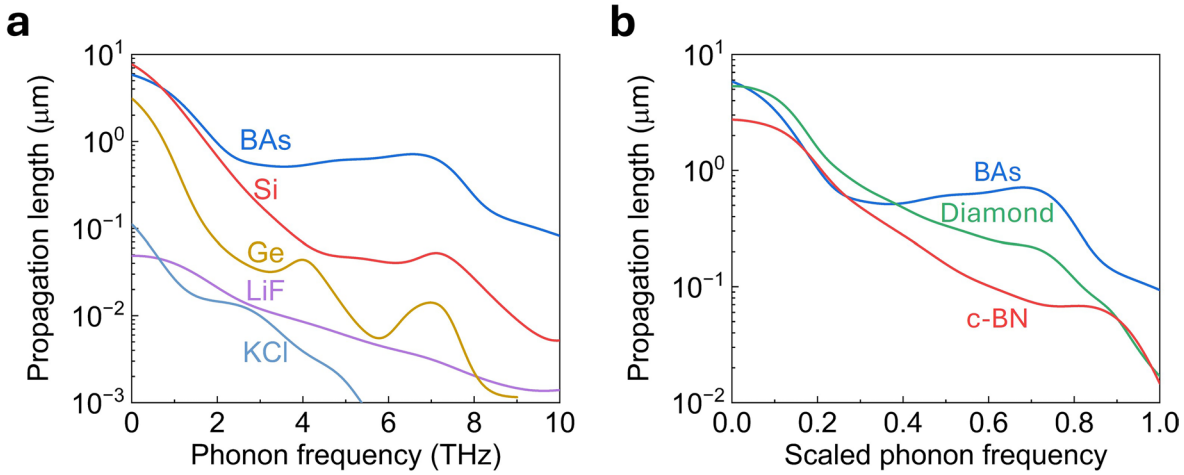

Extended Data Fig. 9 | Spectral propagation lengths in BAs and other materials. a, Comparison with materials in which phonon focusing has been experimentally observed at cryogenic temperatures. **b**, Comparison with other high-thermal-conductivity materials, with frequency normalized by the maximum frequency of the acoustic phonon modes in each material.

https://doi.org/10.1038/s41567-026-03335-y

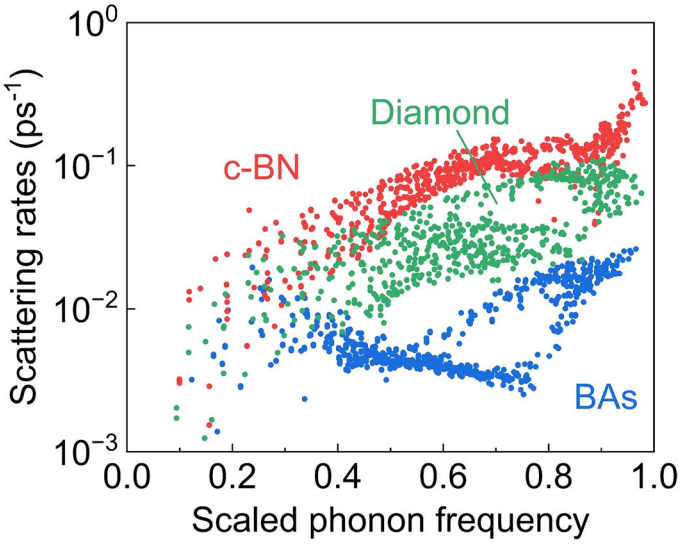

Extended Data Fig. 10 | Mode-dependent phonon scattering rates. Calculated phonon scattering rates are compared among BAs, diamond and cubic boron nitride (c-BN) as a function of normalized phonon frequency.